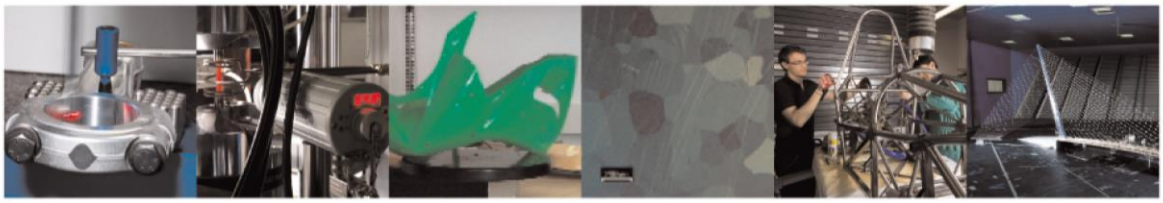

Self-mixing interferometry as a diagnostics tool for plasma characteristics in laser microdrilling

Colombo, Paolo; Demir, Ali Gökhan; Norgia, Michele; Previtali, Barbara

This is a post-peer-review, pre-copyedit version of an article published in OPTICS AND LASERS IN ENGINEERING. The final authenticated version is available online at: http://dx.doi.org/10.1016/j.optlaseng.2016.12.015

Self-mixing interferometry as a diagnostics tool for plasma characteristics in laser microdrilling

Paolo Colombo[1], Ali Gökhan Demir[1]*, Michele Norgia[2], Barbara Previtali[1]

[1]Department of Mechanical Engineering, Politecnico di Milano, Via La Masa 1,

20156 Milan, Italy

[2]Department of Electronics, Information and Bioengineering, Politecnico di Milano, Via Ponzio 34/5, 20133 Milan, Italy

*Corresponding author: aligokhan.demir@polimi.it; Tel: +39 02 2399 8590;

Fax: +39 02 2399 8585

Self-mixing interferometry as a diagnostics tool for plasma characteristics in laser microdrilling

Abstract

In this work, self-mixing interferometry (SMI) was used to monitor the optical path difference induced by the ablation plasma and plume. The paper develops the analytical relationships to explain the fringe appearance in the SMI during laser microdrilling. The monitoring principle was tested under a large experimental campaign of laser microdrilling on TiAlN ceramic coating with a low-ns green fiber laser. Key process parameters namely pulse energy, number and repetition rate were varied. The effect of side gas on the SMI signal characteristic was analysed. Laser induced breakdown spectroscopy (LIBS) was used to identify the plasma temperature and electron number density. The SMI signals were correlated to the plume size and its evolution as a function of process parameters, as well as electron number density estimated by spectroscopy. In addition to proving the validity of the proposed new method, the results show insights to the micromachining of the ceramic material with low ns pulses.

Keywords: Process monitoring, plasma temperature, blast-wave theory, laser microdrilling, ablation

1. Introduction

Lasers are playing a key role in industrial manufacturing as key enabling technologies for precision manufacturing. Micro material processing and marking applications cover 1.28 billion USD revenue worldwide, corresponding to the 41% of the total revenues of laser processing market [1]. Pulsed lasers are fundamental tools for industrial micromachining applications. Nanosecond pulsed lasers are cost effective solutions being widely employed in marking, cutting, drilling and texturing operations. Ultra-fast pulsed lasers operating at ps to fs pulse durations provide superior machining quality and have become much more reliable and affordable in the last few years. With increased reliability of the lasers and reduced costs, more machine tool manufacturers are moving towards adapting these technologies in integrated systems and lasers are expanding their market beyond the original equipment manufacturers' realm. The importance of integrated monitoring equipment is already apparent and will raise as the need for quality assurance increases in time. On the other hand, laser micromachining relies on the complex ablation phenomenon occurring in a very restricted spatial and temporal window.

Several works are available in literature regarding the observation and monitoring of laser ablation dynamics. The used methods vary and are mainly based on mechanical [2], acoustic [3,4] and optical [5-22] principals. Only a few of these methods can be readily adapted as online industrial process monitoring means. The optical methods provide the flexibility of using either the optical emission of the process or a probe light for the monitoring task. A large amount of literature deals with the optical emission of laser ablation for fundamental studies concerning single pulsed laser material interaction [5]. These works study the evolution of plasma temperature and electron number density as a function of position and time. Using a probe light, plasma, shock wave and plume propagation can be also observed. Using methods such as pump-probe [6], schielleren [7], shadowography [8-10], or digital holography [11-13], researches have indicated critical phenomenon and time instances in single pulsed ablation. However, almost all laser micromachining applications consist of a train of pulses with a certain overlap in space and time. Hence, plasma characteristics, shock wave propagation, plume and material ejection vary according to how the pulse train is applied on the material surface. Moreover, the proposed methods require complex optical arrangements and are not easy for implementing on an industrial machine tool. An industrial monitoring tool is expected to be non-intrusive on the machine tool and should preferably use the existing optical chain. From this point use of photodiodes for observing process emission stands out as an appealing option [14]. However, the choice of monitoring wavelength bandwidth is dependent on used material.

In the meantime, interferometric methods have emerged for direct monitoring of the ablated region geometry. In particular, ablation depth monitoring by Fourier domain optical coherence tomography (FT-OCT) [15,16] and self-mixing interferometry (SMI) [17-19] have been demonstrated. A certain stability issue regarding the SMI depth measurements was found, since ablation depth measurements could be possible only in the presence of a side gas [19]. The stability issue concerned the change of SMI signal behaviour, and was attributed to the local variations of the refractive index caused by the ablation plasma and plume [20]. From another point of view, the SMI can be used to interact with the ablation plasma and plume as used as a novel monitoring technique. SMI is easy to implement in existing optical chains of the machining equipment. The information regarding plasma characteristics can be used to ensure the micromachining quality, since plasma and particle shielding as well as heat accumulation are known to reduce machining quality and efficiency [21,22].

Accordingly, this work investigates the use of SMI as a potential monitoring device for ablation plasma characteristics in laser microdrilling. In particular, the SMI measurements are correlated to the plasma characteristics measured via laser induced breakdown spectroscopy. The work initially describes the theory behind the monitoring principle. In the experiments the SMI signal characteristics under different process conditions are analysed in order to confirm feasibility of the monitoring principle. In a large experimental campaign, laser percussion drilling on TiAlN ceramic coating was carried out. SMI signals were acquired as well the emission spectra. The hole depths were measured with focus variation microscopy, optical path change was calculated from the SMI signals and plasma temperature and electron number density were estimated from the emission spectra. The results show the feasibility of the proposed method as well as providing insights to the physical phenomenon occurring during the microdrilling process.

2. Theory

SMI method has been previously employed in laser microdrilling for ablation depth monitoring, where plasma related phenomenon occur contemporarily. The feasibility of monitoring plasma characteristics instead of the ablation depth progression should be demonstrated theoretically and experimentally. Therefore, in the following, the SMI working principle for plasma monitoring purpose is explained. Spectroscopy is also employed in the present work in order to correlate the plasma characteristics measured by a more conventional system to SMI signals. Hence, the basic theory for laser induced breakdown spectroscopy (LIBS) is also explained.

2.1. Working principle of self-mixing interferometry

Conventional interferometry technique used for displacement measurement (Michelson interferometry) uses a reference and a measurement arm. Moreover, the displacement direction is ambiguous. SMI exploits interference occurring in the laser cavity due to back-reflected light. Conventionally, laser diodes (LD) are employed to construct self-mixing interferometers. The photodiodes (PD) for monitoring output power attached to the back of the laser diode is used to measure the power fluctuations due to the interference. In a SMI configuration, the power back reflected from a remote target enters the cavity after being attenuated in the external cavity. The reflected laser field is phase shifted depending on the distance of the reflecting body [23,24]. In SMI, the back reflected field E_r, adds to the lasing field E_l, modulating its amplitude and frequency. The interferometric phase can be retrieved from the change of the optical power, measured by the monitor photodiode. The periodic function of the

interferometric phase, hence the signal shape depends on the feedback parameter (C). When operating in moderate feedback regime ($1<C<4.6$), the signal shows saw-tooth shape, as a fringe is formed at each passage of half-wavelength ($\lambda/2$). Moreover, due to the signal asymmetry, the displacement direction is sensed along with amplitude. The displacement (Δp) can be calculated by counting the number of fringes (n_{frg}):

$$\Delta p = n_{frg} \cdot \lambda/2 \quad (1)$$

As a matter of fact, the displacement sensed by an interferometer is the result of the change in the optical path (p). The optical path change can be induced by a change of distance (d) as well as a change in refractive index of the media (n). Thus, SMI can be used to measure the change in refractive index too [25]. As schematically represented in Figure 1, ablation process generates ablation plume. The plume consists of a plasma core, expanding wavefront and ejected material. All these factors contribute to the change in the refractive index on the material surface, in the proximity to the ablation process. For a stationary target the initial optical path (p_0) can be expressed as:

$$p_0 = d_0 n_1 \quad (2)$$

where d_0 is the distance between the interferometer and the target, and n_1 is the refractive index of the surrounding media. If the refractive index changes locally due to perturbations in the surrounding media, the optical path (p_1) is equal to:

$$p_1 = d_1 n_1 + d_2 n_2 \quad (3)$$

with

$$d_0 = d_1 + d_2 \quad (4)$$

where d_1 is the distance between the interferometer and the perturbed zone, d_2 is the length of the perturbed zone and n_2 is its refractive index. In this work, the perturbed zone corresponds to the ablation plume. Accordingly, the optical path difference between the two instances (Δp) can be calculated as:

$$\Delta p = p_1 - p_0 = d_1 n_1 + d_2 n_2 - d_0 n_1 \quad (5)$$

hence,

$$\Delta p = d_2 \Delta n \quad (6)$$

where Δn is the change in the refractive index. Eq.(6) holds in the case of a stationary target. Therefore, the SMI should not measure the vibrations due to the ablation process. Additionally, both d_2 and Δn are time dependant,

which are held constant in this analytical expression. Previous studies showed that ablation depth measurements with SMI in the absence of a side gas jet was not feasible [19]. Therefore, in the absence of a gas jet, the SMI beam is expected to interact with the ablation plume allowing the functioning of the proposed monitoring scheme.

Figure 1. Schematic representation of the optical path change induced by the ablation plume during laser microdrilling.

2.2. Laser induced breakdown spectroscopy

For plasma temperature (T [K]) and electron number density (N_e [cm^{-3}]) estimation, the local thermal equilibrium (LTE) should be fulfilled [5]. The McWhiter criterion shows the critical electron density to satisfy LTE:

$$N_e \geq 1.6 \cdot 10^{12} T^{0.5} (\Delta E)^3 \quad (7)$$

where ΔE is largest energy gap between the upper and lower energy levels. During the study the largest energy gap for Ti I was 3.834 eV at 323.28 nm transition wavelength. On the other hand, Boltzmann plot method was used to estimate plasma temperature. For of a given specie Boltzmann equation takes the following form:

$$\ln\left(\frac{I_{ji}\lambda_{ji}}{A_{ji}g_j}\right) = -\frac{1}{kT}E_j + \ln\left(\frac{hcN_e}{Z(T)}\right) \quad (8)$$

where I_{ji} denotes the relative intensity of plasma emission of an emission line corresponding to the transition level from i to j, λ_{ji} is the transition wavelength, A_{ji} is the transition probability, g_j is the degeneracy level of level j, $Z(T)$ is the partition function as a function of plasma temperature T, and E_j is the upper level energy. In this equation, I_{ji} and λ_{ji} are obtained through spectroscopy measurements, whereas A_{ji}, g_j and E_j are tabulated data obtained from NIST database [26]. The data was collected for 7 emission line belonging to Ti I as reported in Table 3. The Plank's constant k, Bolzmann's constant h, and speed of light c are known parameters. Using Eq.2 a plot can be constructed with E_j on the abscissa and the logarithmic expression on the left hand side of the equation on the ordinate, a linear fit can be obtained, whose slope yields the temperature. For estimating the electron number density, the Saha-Boltzmann two-line method can be used. If the plasma temperature is known the electron number density can be calculated as:

$$Ne = \frac{I_{ji}^{z}}{I_{ji}^{z+1}} \frac{\lambda_{ji}^{z} A_{ji}^{z+1} g_j^{z+1}}{\lambda_{ji}^{z+1} A_{ji}^{z} g_j^{z}} \cdot 2\frac{(2\pi mk)^{3/2}T^{3/2}}{h^3} \exp\left[\frac{1}{kT}(E_j^{z} - E_j^{z+1} - \chi^{z})\right] \quad (9)$$

where z corresponds to the lower ionization state, χ_z is the ionization energy of the species in the ionization stage z, and m to the mass of an electron. Using the intensities of two ionization species such as Ti I and Ti II, and the plasma temperature estimated with Boltzmann plot method, electron number density can be calculated.

3. Experimental details

The experimental phase was conducted in order to assess several points regarding the use of SMI in plasma monitoring, which can be summarized as the following:

- Microhole geometry and plasma characteristics as function of process parameters.
- Proof of SMI interaction with the plasma plume.
- Correlation between LIBS and qualitative data concerning the microholes with SMI measurements. Further development of SMI measurements for plume propagation.

In the following the materials and systems used in the investigation are explained.

3.1. Material

The monitoring system was evaluated during the percussion microdrilling of TiAlN ceramic coating deposited on AISI D2 tool steel (Balinit Lumena from Oerlikon Balzers, Balzers, Liechtenstein). The coating thickness was measured as 12.1 ± 0.7 µm. Measured average surface roughness was 0.15 ± 0.02 µm.

3.2. Processing laser and self-mixing interferometer

The used processing laser was a master oscillator power amplifier (MOPA) fibre laser operating with green wavelength (YLPG-5 from IPG Photonics, Oxford, MA, USA). The estimated maximum peak and measured maximum average powers are 16 kW and 6 W respectively. The SMI used in this work was constructed using off-the-shelf components. The design criteria are explained in detail elsewhere [19]. A GaAlAs laser diode with a multi-quantum well structure (HL7851G from Hitachi, Ibaraki, Japan) was used as light source. Emission wavelength of the interferometer was 785 nm. The bandwidth (BW) of the interferometer was 1 MHz. SMI was operated at 25°C. The laser diode was injected with 70 mA current that generated about 15 mW optical power.

Depending on the feedback parameter, the self-mixing interference caused a ±0.1 mW fluctuation in the optical power, which was measured as current fluctuation up to 10 μA by the measurement photodiode. Signals were acquired with a digital oscilloscope characterized by 350 MHz maximum bandwidth, 5 GS/s sampling rate and $16 \cdot 10_6$ record length (TDS5034B from Tektronix, Oregon, USA). The beam of the self-mixing interferometer was combined with the processing beam with a dichroic mirror (DMLP567 from Thorlabs, Newton, NJ, USA). The beams were focused using an achromatic lens with 100 mm focal length (AC254-100-A-ML from Thorlabs) and launched onto the workpiece on the same point (see Figure 2). The main specifications of the processing and measurement lasers are summarized in Table 1.

Optical emission of the process was acquired by a spectroscope (Avaspec 2048 USB-2 from Avantes, Apeldoorn, The Netherlands). The wavelength acquisition range was between 200 nm and 1100 nm with 0.575 nm resolution and 1.1 ms minimum integration time. A shortpass optical filter was employed to suppress the processing laser light (500 nm OD2 Shortpass Filter from Edmund Optics, Barrington, NJ, USA). Spectral analyses were carried out between 300 nm and 510 nm. In this wavelength range the emission spectra were corrected using the transmission curve of the optical filter.

Table 1. Main characteristics of the processing and measurement lasers.

Parameter	Processing	Measurement
Emission wavelength, λ	532 nm	785 nm
Emission type	Pulsed wave	Continuous wave
Output power, P	6 W (Average)	0.015 W
Pulse duration, τ	1.2 ns	n/a
Pulse repetition rate, PRR	20-300 kHz	n/a
Maximum pulse energy, E_{max}	20 μJ	n/a
Beam quality factor, M_2	1.1	1.2
Collimated beam diameter, d_c	3.49 mm	2.9 mm (fast axis) 5.1 mm (slow axis)
Focused beam diameter (f=100 mm), d_0	21.7 μm	41.4 μm (fast axis) 23.5 μm (slow axis)

A CCD camera was integrated to the system to take sample images of the ablation plume with and without the gas jet (STC-B33USB-AS from Sentech, Carrollton, TX, USA). The camera was positioned parallel to the material surface (see Figure 2.b) and used with magnification optics as well as filters to attenuate the process emission (NE30A from Thorlabs), as well as the laser light (500 nm Shortpass Filter OD2 from Edmund Optics).

The maximum temporal resolution of the device was 121 fps. The images were acquired with 60 fps, resulting in integration of the process to a single frame. A signal generator was used for triggering the components at the same time (AFG310 arbitrary function generator from Sony-Tektronix, Wilsonville, OR, USA).

Figure 2. Schematic representation of the experimental setup. a) Coupling of processing and SMI beams, and spectroscopy sections. b) CCD camera section.

3.3. Experimental plan

Laser percussion microdrilling was the used processing strategy. Experiments were carried out with fixed focal position (h_f) on material surface. Key process parameters namely, pulse energy (E), number of pulses (N) and pulse repetition rate (PRR) were varied in order to obtain different hole diameters (D) and depths (h) with different drilling times (t_{drill}). Each condition was replicated 5 times. All experiments were carried out with N_2 side gas flowing at 1 bar parallel to the material surface in order to interact with the plasma and plume. The details of the experimental campaign are summarized in Table 1. The hole morphology was analysed by scanning electron microscopy (EVO-50 from Carl Zeiss, Oberkochen, Germany) images. Hole depth (h) was measured with focus variation microscopy (Infinite Focus, Alicona Imaging, Graz, Austria). SMI as well as breakdown spectroscopy was employed during all the experiments. The SMI signals were initially characterized in terms of shape, amplitude and feedback regime and compared to conditions with the use of side-gas. The rise time (t_{rise}) of the signals was measured and compared to the drilling time. The rise time is defined as the time elapsed for reaching the maximum displacement, measured by the SMI. The maximum optical path difference (Δp_{max}) reached by the end of the microdrilling process was also assessed.

Table 2. Experimental plan for accuracy evaluation of the monitoring system.

Fixed parameters		
Focal position	h_f [mm]	0
Varied parameters		
Pulse energy	E [µJ]	5, 10, 15, 20
Number of pulses	N [-]	50, 100, 150, 200, 250
Pulse repetition rate	PRR [kHz]	160, 300

Emission spectra were acquired with 10 ms integration time. This duration was longer than the longest drilling time, hence, a single spectrum was registered for each single micro hole. The resultant spectrum was integrated the optical emission in the whole microdrilling process time and in space below the field of view. Seven emission line belonging to Ti I as shown in Figure 4 were chosen and related emission data were collected as reported in Table 3. The Boltzmann plot method is sensitive to the selection of the lines. In order to minimize the effect of the selected lines the calculations were repeated 6 times, starting with all the emission lines and excluding one Ti I emission line at a time in the remaining calculations, with *w* being the calculation number. The linear fit conditions showing R^2 values below 75% were excluded from analysis. For machining condition *u* and replicate *v*, *s* number of calculations would exist with $s \leq 7$. The plasma temperature was taken average of these calculations and can be expressed as:

$$T_{u,v} = \frac{1}{s}\sum T_{u,v,w} \tag{10}$$

The intensity of Ti II line at 369.98 nm emission wavelength was used with Ti I line at 335.29 nm (χ_z=6.83 eV). The temperature and electron number density calculations are valid under LTE. However, in order to verify the LTE criteria, these two measures should be known. In this work, the *T* and *Ne* values were calculated first and LTE condition was controlled with these estimates. Only the conditions fulfilling LTE were considered in further analysis. The flow chart of the overall approach is presented in Figure 3.

Table 3. Selected spectral lines and the corresponding spectral data [26].

Specie	λ_{ji} [nm]	A_{ji} [s^{-1}]	E_j [cm^{-1}]	g_j
Ti I	323.28	$2.56 \cdot 10^7$	47030.23	9
Ti I	335.29	$9.70 \cdot 10^5$	29986.20	7
Ti I	350.66	$6.80 \cdot 10^5$	28896.06	11
Ti I	363.79	$9.30 \cdot 10^5$	27480.07	7
Ti I	368.73	$3.68 \cdot 10^5$	27498.98	7
Ti I	497.77	$4.41 \cdot 10^6$	36351.37	11
Ti II	365.98	$1.84 \cdot 10^7$	40074.67	8

Figure 3. Flow chart of the plasma temperature analysis.

4. Results

4.1. Microdrilled hole morphology

Figure 4 shows SEM images of the microdrilled holes. It can be observed that pulse energy results in larger hole diameters, whereas the number of pulses (*N*) provides mainly an increase in hole depth and dross around the hole entry. In terms of hole morphology, pulse repetition rate (PRR) does not show a significant change. The images imply that the process is mainly governed by direct vaporization with little fraction of melt generation between 50-100 pulses for all energy levels. The melt fraction accumulates around the hole edges with increased number of pulses. Large particles and debris are visible when, the energy is between 15-20 μJ and 200-250 pulses are used. These particles appear to be detached parts of the molten phase, rather than products of explosive behaviour. As shown in Figure 5, hole depth (*h*) varies between 1 and 14 μm, therefore below and beyond the coating thickness. Both pulse energy and number of pulses increase the hole depth, whereas pulse repetition rate appears to be not influential.

Figure 4. SEM images of the microholes realized with different parameter combinations. a) Microholes produced with PRR=160 kHz, variable *E* and *N*; b) microholes produced with *PRR*=300 kHz, variable *E* and *N*.

Figure 5. Hole depth (*h*) as a function of process parameter.

4.2. Plasma temperature and electron number density

Figure 6 shows spectroscope acquisitions during the microdrilling of the TiAlN coating. It can be observed that in both the pulse energy (Figure 6.a) and number of pulses (Figure 6.b) increase the emission strength of the Ti I and Ti II peaks. On the other hand, variation of pulse repetition rate (Figure 6.c) did not result in any significant difference between the observed spectra. Out of the 200 acquisitions, 178 passed the criteria depicted in Section 3.3 and were further analysed. Figure 7 shows the estimated plasma temperatures and electron number densities respectively. The plasma temperature was found to vary between 6700 K and 7500 K over the experimented range. On the other hand, the electron number densities varied between $1 \cdot 10_{16}$ and $7 \cdot 10_{16}$ cm^{-3}. Each temperature and electron number density estimate is a mean over space in time during the overall microdrilling operation. Hence, higher values for both of the measures can be expected around the initial stages of the ablation, right after the end of each single pulse close to the ablation zone. The results are comparable to literature data regarding

plasma temperatures estimated in laser microdrilling. Ii et al estimated plasma temperatures between 5000 and 9000 K during percussion microdrilling of steel substrates under He and O_2 with pulse duration between 150 and 500 ns [27].Shin and Mazumder also estimated plasma temperature between 7700 and 9200 K and electron number density between $5 \cdot 10_{15}$ and $8 \cdot 10_{15}$ during trepanning drilling of Inconel 718 [28]. The used laser operated with 150 µs pulse duration.

Regression models were sought to explain the trends observed in the plasma temperature and electron number density estimates. In both cases, no statistical evidence was found for the significance of the pulse repetition rate. In the case of plasma temperature, the regression model was in the following form:

$$T\,[K] = 6294.8 + 92.67\,E\,[\mu J] + 1.708\,N - 1.949\,(E\,[\mu J])^2 - 0.0578\,E\,[\mu J] \cdot N \quad (11)$$

The model fits the data well with R_{2adj} at 86.2%. As also depicted in Figure 7, the increasing number of pulses for a fixed pulse energy level increase the plasma temperature linearly. The slope of temperature increase decreases for higher pulse energy level, which shows a saturation trend. The regression equation for the electron number density has the following form:

$$(Ne[cm^{-3}]) \cdot 10^{-16} = 0.3180\,E\,[\mu J] + 0.00314\,N - 0.00470\,(E\,[\mu J])^2 + 0.000291\,E\,[\mu J] \cdot N \quad (12)$$

with R_{2adj} at 98.5%. Similar to the plasma temperature, the electron number density increases as the number pulses increase for a fixed pulse energy level. However, in this case the slopes also increase as a function of pulse energy, depicting that despite saturating behaviour in the plasma temperature, more material is ionized with higher pulse energy.

Figure 6. Optical emission spectra as a function of process parameters. a) Variable *E* with *N*=250, *PRR*=300 kHz; b) variable *N* with *E*=20µJ, *PRR*=300kHz; c) variable *PRR* with *E*=20µJ, *N*=250.

Figure 7. a) Plasma temperature and b) electron number density as a function of number of pulses and pulse energy. The lines depict the fitted values using the regression model for different energy levels. Data points represent group means ± group standard deviation.

In addition to the overall plasma characteristics, the results also depict the expected trends in the SMI signal evolution. If the SMI signals should be correlated to the plasma quantity, they should increase as function of pulse energy (*E*) and number (*N*), whereas not effected by pulse repetition rate (*PRR*).

4.3. Confirmation of interaction between SMI and ablation plasma

In order to verify the interaction between the SMI and the ablation plasma signal characteristics should be assessed with and without the use of side gas. Figure 8 compares SMI signals obtained with and without the use of a side gas jet employing the same microdrilling parameters (*E*=10 μJ, *PRR*=160 kHz, *N*=150). It can be observed that the SMI signal in the presence of side gas jet shows unidirectional fringes with around 100 mV peak-to-peak amplitude (Figure 8.a). The direction of movement is away from the SMI, confirming that the observed phenomenon is the displacement of the ablation front. The signal appears to be in low-feedback regime, showing reduced feedback parameter, as the saw-tooth shape tends to become more symmetrical. On the other hand, the peak to peak fringe amplitude of SMI signal in the absence of side gas (Figure 8.b) is higher (around 300 mV). In this case, the saw-tooth shape is well defined, confirming the operation in moderate feedback regime. Particularly, the signal shows initially target movement toward the SMI during the drilling operation. Once the drilling is terminated, displacement direction is away from the SMI. The number of fringes on both directions are equal, which results in null total displacement. Accordingly, the SMI signal is not measuring the ablation front displacement, but fringe appearance is caused by another phenomenon. The signal observed in the absence of the side gas shows also superimposed small fringes with higher frequency and smaller amplitude. The zoomed section presented in Figure 8.c shows that the period of the small fringes is close to the one observed in Figure 8.a and they indicate an opposite movement direction compared to the larger fringes. It can be deduced that the SMI signal, in the absence of gas, carries information regarding both ablation front displacement and another ablation related phenomenon causing a change in the optical path. However, the signal quality is not always adequate to resolve the signal component belonging to the ablation front displacement.

The change in signal characteristics due to the use of the side gas was initially attributed to two possible mechanisms in previous work [19]: i) deviation of ablation plasma and plume from the hole opening by the gas

jet; ii) extinguishing effect of the gas jet on the plasma. Mezzapesa et al. [18] observed similar phenomenon during the ablation depth measurement in laser percussion microdrilling of 50 μm-thick Al sheets. The authors used a quantum cascade laser for SMI and a ps laser as the machining system. With high laser fluence the authors observed superimposed high and low frequency fringes. The authors attributed the appearance of the low frequency and high amplitude fringes similar to the ones seen in Figure 8.b to the thermal deformation. Fringes with smaller amplitude and higher frequency, similar to the ones in Figure 8.c, were present in the signal, which were linked to the actual ablation front displacement. The authors could obtain stable SMI signals showing only ablation front displacement by lowering the laser fluence. Such thermal deformation is not expected to be the cause of the formation of large fringes in this work, when the side gas is absent. The higher total thickness (12 mm) of the used specimens and machining on hard ceramic coating with high stiffness are expected to prevent pronounced thermal deformations. On the other hand, Sjödahl et al. applied laser speckle correlation to measure the surface deflections during laser microdrilling of metallic targets. The authors reported 50 nm of deflection on the back side of 0.5 mm thick copper plates after drilling more than half the thickness of the plate [29]. Hence, the expected surface deformation is less than an amount able to form a complete fringe (<393 nm). Moreover, the use of the side gas changes the signal behaviour in the same processing conditions. The side gas alone is not expected to prevent thermal deformations on the material surface with the low pressure and flow provided.

Figure 8. SMI signal characteristics observed during microdrilling with and without the use of side gas (*E*=10 μJ, *PRR*=160 kHz, *N*=150). a) Signal observed during the drilling time when the side gas is used. b) Signal observed without the use of side gas during the drilling time and beyond, black square showing the zoomed section. c) The zoomed portion of the signal showing superimposed small fringes.

Figure 9.CCD camera images of the ablation plume a) with and b) without gas flow.

In order to comprehend the effect of the side gas CCD camera images were acquired with and without its use. Figure 9 demonstrates the results obtained. The captured images are integrated over the whole drilling time. The images clearly show the change of direction around the higher part of the ablation plume. The measurement of the ablation depth is possible, since the SMI beam passes only partially through the ablation plume when the side

gas is used. Instead, when the side gas is absent, the SMI beam will completely interact with the ablation plasma and plume. These observations are coherent with literature. Local changes in refractive index due to laser ablation has been reported in different studies [6-13]. These studies show that under the influence of a single pulse, the refractive index around the machining zone can vary around 0.001 due to the shock wave, plasma and plume formation. Material ejecta and vapour around the ablation zone are also disturbance factor changing the refractive index [6,30]. Both material ejection and vapour can last even after the ns-pulse duration up to µs second regime. The use of multiple pulses, which is required for the percussion drilling, generates further accumulation of all the observed changes around the ablation zone. Pangovski et al. [31] studied the effect of multiple pulses on Si target with 25 kHz pulse repetition rate and 250 ns duration. The work shows that the consecutive pulses arrive during the expansion of the shock wave resulting from the previous pulse. The resulting plasma front of the consecutive pulses generate other shock wave fronts propagating within the previous one. With the increasing number of pulses, the shock wave front and plume accumulate. With a single pulse, the shock wave propagation shows spherical symmetry, whereas with multiple pulses the zone with refractive index change grows larger (>1.8 mm) and elongates perpendicular to the surface. Such elongated laser induced plume is also a common phenomenon in laser welding. The laser induced plume is found to decrease welding penetration by scattering the processing beam [32,33]. The use of fan or side gas jet has been effective to reduce and remove the plume column, whereas the plasma core was found to remain present around the welding zone.

Another important signal characteristic was found to be the correlation between the rise time (t_{rise}) of the SMI signal and the drilling time (t_{drill}) as seen in Figure 8.c. Figure 10 exhibits the measured rise times as a function of chosen drilling times within the experiments. The regression model fitted to the data confirm the correlation with the following equation:

$$t_{rise}\ [ms] \ = \ 1.006 \cdot t_{drill}\ [ms] \tag{13}$$

The equation fits the data very well with R_{2adj}=99.6%. This correlation shows that the optical path difference increases only during the laser emission and decreases right after it, such as the accumulation of ablation plume.

In the light of the measurements and the reported data from the literature, it is concluded that the side gas removes the ablation plume and in its absence the SMI interacts with the ablation plume. Hence, the fringes appearing in

the SMI signal in the absence of the side gas are due to the refractive index changes around the ablation zone. The null total displacement is the results of the formation of the ablation plume during the process and its dissolution after the drilling time. A final comment regards the SMI fringes amplitude: the interferometric fringes induced by the hole growth show a lower amplitude, because the hole diameter (10-22 μm) is lower than the interferometer laser spot diameter (41.4 μm in fast axis, 23.5 μm in slow axis). The returning light with phase-shift is therefore only a fraction of the back-scattered light. When considering a change in the refraction index, instead, almost all the interferometer beam is involved. Due to the linearity of the self-mixing effect, both the effects can happen together (see Figure 8.b and c).

Figure 10. Measured rise times as a function of the drilling time.

4.4. Use of the self-mixing interferometry signals for plasma monitoring

The displacement measured by the SMI or the change in optical path length can be also calculated using Eq (1). Incomplete fringes were compared to complete fringes in amplitude to estimate the corresponding optical path difference by proportion. Assuming that the optical path change is due to the change of refractive index only, it is possible to calculate the plume size (d_2) rewriting Eq.(6). For this purpose, the change of refractive index (Δn) around the ablation region was estimated from data coming from literature. Using the refractive index profiles obtained during single pulsed ablation of Ti [11] and Si targets [34], the weighted average of refractive index change was estimated as 0.00027941 and 0.000257475 respectively. In both of the works, the probe laser wavelength was 532 nm. The refractive index of non-disturbed air does not vary significantly for the SMI wavelength (785 nm). However, the refractive index of the ablation zone may vary for the wavelength used here and the calculation are indicative only. The values depict that in the ablation zone an overall increase of refractive index is expected. This is due to the fact that the extent of plasma shock wave is usually larger than the one belonging to the plasma zone.

Figure 11 reports the evolution of the plume size as a function of time for an example microdrilling condition (E=10μJ, PRR=160 kHz, N=200). The graph reports the unwrapped SMI signal multiplied by the refractive index change values found in the literature. It can be observed that the plume extension increases asymptotically. In the

experiments, between 1 to 4 fringes were visible as a function of process parameters. This corresponds to optical path changes between about 0.4 μm and 1.6 μm. The corresponding plume size on the other hand varies between 0.7 and 6 mm. Such dimensions of ablation plume are realistic for ablation with multiple pulses, as also demonstrated by holographic images in Ref. [31].

Figure 11. Example of SMI signal evolution and corresponding interval of plume size calculated using refractive index values reported in [11] and [34]. Process parameters are *E*=10μJ, *PRR*=160 kHz, *N*=200.

Similar to the plasma characteristics, the optical path difference measured by the SMI was found to not depend on pulse repetition rate. The data presented in Figure 12 shows the progression of the optical path difference as a function of number of pulses for each pulse energy group. The present data follows a trend that can be expressed with a power function. Hence, instead of fitting a global regression equation, for each pulse energy level a separate model was fitted following the generic form of:

$$\Delta p_{max} = C \cdot N^{x} \tag{14}$$

Eq.(14) expresses also the trend in maximum plume size ($d_{2,max}$) according to Eq.(6). As reported in Table 4, between 5 μJ and 15 μJ the data points are fitted well with the exponent around between 0.36 and 0.55. Such trends have been reported for the shockwave expansion in single pulsed laser ablation. According to the Sedov-Taylor blast wave theory, after the initiation a sudden explosion, the shock wave front propagation in time (t) is proportional to t_x [35,36]. The exponent x defines the propagation symmetry, where x=0.4 stands for spherical, x=0.5 for cylindrical and x=0.66 for planar propagations. For single pulsed ablation with high energy densities, several groups reported that the shock wave follows a spherical propagation in time. The use of this model in the present case shows differences due to the use of a train of pulses and use of number of pulses instead of time in the analysis. The resultant fits show that the propagation of the ablation products that change the refractive index caused by a train of sudden explosions follow a cylindrical propagation with lower energy levels (5-10 μJ) and moves towards a spherical propagation with higher energy levels (15-20 μJ). A cylindrical propagation is caused by a linear heat source and the propagating shock wave front is elongated around the surface normal, depicting an

energetic equilibrium around this axis. This description fits well with the observed morphology in Figure 9. A spherical expansion is caused by a point source, which corresponds to a non-equilibrium state in all directions of the source. The occurrence of spherical expansion of the laser ablation induced shock wave has been reported with high intensity pulses in ns regime [9,11,12]. The ablation conditions often yield breakdown in air and laser supported detonation, which all reduce quality in laser micromachining. On the other hand, with lower energy intensities the shock wave expansion behaviour was observed to deviate from spherical towards planar [13]. The occurrence of planar shock wave expansion was also linked to better machining conditions [37]. The results of this work imply that the optical path distance caused by refractive index change follows a trend similar to cylindrical expansion as a function of increased number of pulses. With increased laser power, hence energy density, the conditions move towards spherical expansion, which can be an indicator to the deteriorating machining quality as a function of number of pulses for pulse energy at 20 µJ. Another important factor is that the propagation of the zone with refractive index change depends on the number of pulses but not on time. Operating at 160 kHz and 300 kHz the period for each pulse is 6.25 µs and 3.33 µs respectively. For ns-pulsed laser ablation, such time intervals are too long for each pulse to impact on the previous plasma core, which finishes with ns time scale [8,30]. In µs time scale material droplets are still ejected from the surface as the shock wave propagation continues [6,10,13,30]. Apparently, the reduction of the temporal distance with the increased pulse repetition rate does affect the shock wave propagation or the material ejection characteristics either. This is coherent with the hole morphologies, measured depths, plasma temperatures and electron number density. On the other hand, the increase of pulse repetition rate has been shown to reduce ablation efficiency due to plasma and particle shielding as well as heat accumulation. König et al predicted this effect during the single pulsed ablation [22]. The authors suggested the use of a few hundreds of kHz to avoid plasma and particle shielding. Later on, Ancona et al showed reduction of efficiency with high pulse repetition rates in laser percussion microdrilling of steel substrates with fs pulses [38]. More recent studies showed that such effect is absent on some metals during laser engraving [39]. This implies that spatial overlapping is a key factor as well as the temporal one. In the case of ns-pulsed laser microdrilling, Jackson and O'Neill observed a reduction in the drilling etch rate with the increase of pulse energy [40]. The authors operated at 1 kHz pulse repetition rate on M2 tool steel, and attributed the loss of efficiency to plasma shielding. Reduction of processing efficiency due to increased pulse repetition

rate has not been observed with ns pulses, also due to the fact that these lasers commonly operate up to a few hundreds of kHz. It can be concluded that the analysis of the SMI measurements are coherent with what has been previously reported in literature, as well as the LIBS measurements.

Figure 12. Optical path difference measured by the SMI and calculated plume size as a function of process parameters. The lines depict the fitted regression models for different energy levels. Data points represent group means ± group standard deviation.

Table 4. Coefficients of the Eq.(13) fitted for different laser energy groups. Values are reported with expected value of the regressor ± 95% confidence interval.

E [µJ]	x	C
5	0.48±0.13	54±28
10	0.54±0.09	63±24
15	0.45±0.09	121±40
20	0.36±0.08	193±64

Finally, a direct relationship between the plasma characteristics measured by LIBS and SMI was assessed. As shown in Figure 13, optical path difference measured by SMI is correlated to electron number density with a power function expressed by the following equation:

$$\Delta p_{max}[nm] = 369 \cdot (Ne[cm^{-3}] \cdot 10^{-16})^{0.68} \quad (15)$$

The model fits the data adequately with a high R_{2adj} at 95.9% and exhibits clearly that the plasma quantity increases the optical path difference. In addition to the confirmation of the phenomenologically modelled physical phenomenon, this result shows the potentiality of the use of SMI for an indirect quantification the ablation plasma.

Figure 13. Relationship between the electron number density and optical path difference measured by the SMI.

5. Comparison of SMI with conventional methods as a potential industrial plasma monitoring tool

The demonstrated use of SMI combines advantages of different monitoring devices, more specifically the ones using spectroscopy or fast photodiodes. Photodiodes are not selective in measurement wavelength unless optical filters are used. If the plasma emission is needed to be monitored, conventional photodiodes can either integrate the whole spectrum intensity or observe a certain region of the spectrum. The integrated spectrum gives only a

generic idea of process drifts. Selection of emission band is required for specific material to be machined according to its plasma emission characteristics. The photodiode response also needs to be matched to the process quality, requiring the calibration of the monitoring device. In order to quantify the plasma characteristics through analytical models, multiple photodiodes may be required to increase wavelength resolution. Spectroscopes provide wavelength rich information, but are commonly slow in temporal scale. The information can be used to estimate plasma properties, beyond the use of the signal in a black-box control scheme. The plasma diagnostics carried out by SMI provides temporal resolution of a photodiode, its implementation is independent from the plasma emission characteristics of the material and can be used to quantify the plasma. Additionally, the plume dimension can be estimated. These features render SMI as a flexible device for monitoring laser micromachining quality of different materials, through plasma characteristics. On the other hand, SMI is prone to mechanical disturbances. External vibrations can be measured through the device, which can be filtered out later on. While photodiode and spectroscopy alignment may be less critical due to large sensors, misalignment of the SMI beam generates signal decay and loss.

6. Conclusions

This works presents the use of SMI as a diagnostics tool for ablation plasma in laser microdrilling. The analytical developed analytical model expressed the SMI signal formation due to the change in refractive index rather than the movement of the target as in Eq.(6). The experimental analysis confirmed that the signal formation is due to the refractive index change in the absence of a side gas during the laser microdrilling process. In summary, SMI was found to be rich in information providing measurements of process duration, plume size, expansion symmetry and indirect measurement of the electron number density. In particular, the increase in the optical path difference could be approximated with the blast wave theory. The results showed that the time component of the blast wave theory could be substituted with number of pulses as no temporal influence due to the change in pulse repetition rate was observed. The data showed the presence of a cylindrical expansion that is coherent with the observed shape of the ablation plume. The changes in the expansion behaviour was also linked to machining quality, where a spherical expansion component was observed for microdrilling conditions producing higher material deposit around the holes. The dimensions of the zone with refractive index change was estimated using the refractive

index changes reported in literature. The extension of this zone was found to vary between 1-6 mm, which is coherent with the observations reported in literature. Finally, the plasma electron number density was correlated to the change of optical path distance following a power function.

This study confirms the feasibility of using SMI as a diagnostics tool for plasma characterisation, as well as providing the preliminary analysis on an industrial micromachining process. The SMI simplicity makes it a cost effective and easy-to-implement option for process monitoring. It is also possible to extend the use of this approach to monitor plasma characteristics in other industrial manufacturing processes, such as laser cutting and welding. However, speckle effects due to the moving target is a potential issue that needs to be taken into account both in optical design and signal analysis phases.

Acknowledgements

The authors express their gratitude to IPG Italy for providing the green fiber laser source.

References

1. Belforte DA. 2015 industrial laser market outperforms global manufacturing instability. *Industrial Laser Solutions* 2015; 31(1): 6-11
2. Stafe M, Negutu C, Popescu IM. Real-time determination and control of the laser-drilled holes depth. *Shock Waves* 2005; 14(1–2):123–126
3. Bordatchev EV, Nikumb SK. Information properties of surface acoustic waves generated by laser-material interactions during laser precision machining. *Meas. Sci. Technol* 2002; 13:836–845
4. Stournaras A, Chryssolouris G. On acoustic emissions in percussion laser drilling. *Int. J. Adv. Manuf. Technol.* 2010; 46(5–8):611–620
5. Aragón C, Aguilera JA. Characterization of laser induced plasmas by optical emission spectroscopy: A review of experiments and methods. Spectrochim. Acta - Part B At. Spectrosc. 2008; 63(9):893–916
6. Jeong SH, Greif R, Russo RE. Shock wave and material vapour plume propagation during excimer laser ablation of aluminium samples. J. Phys. D. Appl. Phys. 1999; 32(19):pp. 2578–2585, Oct. 1999.
7. Callies G, Berger P, Hugel H. Time-resolved observation of gas-dynamic discontinuities arising during excimer laser ablation and their interpretation. *J. Phys. D. Appl. Phys*. 1995; 28(4):794–806
8. Zeng X, Mao XL, Greif R, Russo RE. Experimental investigation of ablation efficiency and plasma expansion during femtosecond and nanosecond laser ablation of silicon. *Appl. Phys. A* 2004;80(2): 237–241
9. Gravel JFY, Boudreau D. Study by focused shadowgraphy of the effect of laser irradiance on laser-induced plasma formation and ablation rate in various gases. *Spectrochim. Acta Part B At. Spectrosc*., 2009; 64(1):56–66
10. Zhou Y, Wu B, Tao S, Forsman A, Gao Y. Physical mechanism of silicon ablation with long nanosecond laser pulses at 1064nm through time-resolved observation. *Appl. Surf. Sci.* 2011; 257(7): 2886–2890
11. Amer E, Gren P, Kaplan FH, Sjödahl M, El Shaer M. Comparison of the laser ablation process on Zn and Ti using pulsed digital holographic interferometry. *Appl. Surf. Sci*. 2010;256(14): 4633–464

12. Amer E, Gren P, Sjödahl M. Laser-ablation-induced refractive index fields studied using pulsed digital holographic interferometry. *Opt. Lasers Eng.* 2009; 47(7–8):793–799
13. Demir AG, Pangovski K, O'Neill W, Previtali B. Investigation of pulse shape characteristics on the laser ablation dynamics of TiN coatings in the ns regime. *J. Phys. D. Appl. Phys.* 2015;48:235202 (11pp)
14. Stournaras A, Salonitis K, Chryssolouris G. Optical emissions for monitoring of the percussion laser drilling process. *Int. J. Adv. Manuf. Technol.* 2009;46(5–8): 589–603
15. Webster PJL, Wright LG, Mortimer KD, Leung BY, Yu JXZ, Fraser JM. Automatic real-time guidance of laser machining with inline coherent imaging. *J. Laser Appl.* 2011;23(2): 022001
16. Webster PJL, Yu JXZ, Leung BYC, Anderson MD, Yang VXD, Fraser JM. In situ 24 kHz coherent imaging of morphology change in laser percussion drilling. *Opt. Lett.* 2010; 35(5): 646–648
17. Mezzapesa FP, Ancona A, Sibillano T, De Lucia F, Dabbicco M, Lugarà PM, Scamarcio G. High-resolution monitoring of the hole depth during ultrafast laser ablation drilling by diode laser self-mixing interferometry. *Opt. Lett.* 2011; 36(6):822–824
18. Mezzapesa FP, Spagnolo V, Ancona A, Scamarcio G. Detection of ultrafast laser ablation using quantum cascade laser-based sensing. *Appl. Phys. Lett.* 2012;101(17):171107
19. Demir AG, Previtali B, Magnani A, Pesatori A, Norgia M. Application of self-mixing interferometry for depth monitoring in the ablation of TiN coatings. *J. Laser Appl.* 2015; 27(S2): S28005
20. Demir AG, Colombo P, Norgia M, Previtali B. Evaluation of Self-Mixing Interferometry Performance in the Measurement of Ablation Depth. *IEEE Trans. Instrum. Meas.* 2016; 65(11): 2621-2630
21. Li C, Vatsya SR, Nikumb SK. Effect of plasma on ultrashort pulse laser material processing. *J. Laser Appl.* 2007; 19(1):26
22. König J, Nolte S, Tünnermann A. Plasma evolution during metal ablation with ultrashort laser pulses. *Opt. Express* 2005; 13(26):10597–10607
23. Giuliani G, Norgia M, Donati S, Bosch T. Laser diode self-mixing technique for sensing applications. *J. Opt. A Pure Appl. Opt.* 2002; 4(6):S283–S294

24. Donati S. Developing self-mixing interferometry for instrumentation and measurements. *Laser Photon. Rev.* 2012;6:393-417

25. Taimre T, Nikolić M, Bertling K, Lim YL, Bosch T, Rakić AD. Laser feedback interferometry: a tutorial on the self-mixing effect for coherent sensing, *Adv. Opt. Photonics* 2015;7(3):570-631

26. Kramida A, Ralchenko Y, Reader J, NIST ASD Team. NIST Atomic Spectra Database (ver. 5.3) [Online]. http://physics.nist.gov/asd [accessed 11.01.16]

27. Ii M, Duffey TP, Mazumder J. Spatially and temporally resolved temperature measurements of plasma generated in percussion drilling with a diode-pumped Nd : YAG laser. *J. Appl. Phys.* 1998; 84(8):4122–4127

28. Shin J, Mazumder J. Plasma diagnostics using optical emission spectroscopy in laser drilling process. *J. Laser Appl.* 2016;28(2): 022008

29. Sjödahl M, Gren P, Sárady I, Miroshnicova N. Laser hole drilling process studied using laser speckle correlation. *Proc. SPIE* 2006; 6341: 63412M

30. Russo RE, Mao XL, Liu HC, Yoo JH, Mao SS. Time-resolved plasma diagnostics and mass removal during single-pulse laser ablation. *Appl. Phys. A* 1999;69 [Suppl.]: S887–S894

31. Pangovski K, O'Neill W, Teh PS, Richardosn D, Demir AG. Designer pulses for precise machining of silicon – A step towards photonic compositions. *Proc. ICALEO* 2012:999–1008

32. Oiwa S, Kawahito Y, Katayama S. Optical properties of laser-induced plume. *Proc. ICALEO* 2009:359–365

33. Wang CM, Meng XX, Huang W, Hu XY, Duan AQ. Role of side assisting gas on plasma and energy transmission during CO_2 laser welding. *J. Mater. Process. Technol.* 2011; 211(4):668–674.

34. Pangovski K, Sparkes M, Cockburn A, O'Neill W, Teh PS, Lin D, Richardson D. Control of Material Transport Through Pulse Shape Manipulation — A Development Toward Designer Pulses. IEEE J of Sel. Top. Quantum Electron. 2014; 20 (5): 51-63.

35. G. Taylor, "The Formation of a Blast Wave by a Very Intense Explosion. II. The Atomic Explosion of 1945," *Proc. R. Soc. A Math. Phys. Eng. Sci.*, vol. 201, no. 1065, pp. 175–186, Mar. 1950.

36. Taylor G. The formation of a blast wave by a very intense explosion I . Theoretical discussion. *Proc. R. Soc. A Math. Phys. Eng. Sci.* 1950; 201(1065):159–174

37. Yavas O, Maddocks E. Planar and spherical shock wave generation during infrared laser ablation of calcium carbonate. *Appl. Surf. Sci.* 1998; 127–129: 26–32

38. Ancona A, Röser F, Rademaker K, Limpert J, Nolte S, Tünnermann A. High speed laser drilling of metals using a high repetition rate, high average power ultrafast fiber CPA system. *Opt. Express* 2008;16(12) 8958–8968

39. Neuenschwander B, Jaeggi B, Zimmermann M, Hennig G, Technologies, "Influence of particle shielding and heat accumulation effects onto the removal rate for laser micromachining with ultra-short pulses at high repetition rates. *Proc. ICALEO* 2014:M1104

40. Jackson MJ, O'Neill W. Laser micro-drilling of tool steel using Nd:YAG lasers. *J. Mater. Process. Technol.* 2003; 142(2): 517–525.

List of figures

List of tables